nature synthesis

Article

https://doi.org/10.1038/s44160-024-00643-0

Synthesis pathways to thin films of stable layered nitrides

Received: 17 April 2024

Accepted: 9 August 2024

Published online: 06 September 2024

Check for updates

Andriy Zakutayev[1] ✉, Matthew Jankousky[2], Laszlo Wolf[2], Yi Feng[3], Christopher L. Rom[1], Sage R. Bauers[1], Olaf Borkiewicz[4], David A. LaVan[3], Rebecca W. Smaha[1] & Vladan Stevanovic[2]

Controlled synthesis of metastable materials away from equilibrium is of interest in materials chemistry. Thin-film deposition methods with rapid condensation of vapour precursors can readily synthesize metastable phases but often struggle to yield the thermodynamic ground state. Growing thermodynamically stable structures using kinetically limited synthesis methods is important for practical applications in electronics and energy conversion. Here we reveal a synthesis pathway to thermodynamically stable, ordered layered ternary nitride materials, and discuss why disordered metastable intermediate phases tend to form. We show that starting from elemental vapour precursors leads to a 3D long-range-disordered $MgMoN_2$ thin-film metastable intermediate structure, with a layered short-range order that has a low-energy transformation barrier to the layered 2D-like stable structure. This synthesis approach is extended to $ScTaN_2$, $MgWN_2$ and $MgTa_2N_3$, and may lead to the synthesis of other layered nitride thin films with unique semiconducting and quantum properties.

The controlled synthesis of metastable solid-state materials away from thermodynamic equilibrium using traditional bulk methods presents a substantial challenge[1]. Synthesizing metastable polymeric, metallic and semiconducting materials has important implications for electronic technologies and energy conversion. The reciprocal challenge is how to synthesize thermodynamically stable structures using kinetically limited thin-film deposition methods, which are often used in manufacturing but tend to favour metastable material polymorphs. Among nitride thin films, examples of metastable thin-film materials used for practical applications include MoN as an electrocatalyst for hydrogen evolution[2] and NbN in superconducting qubits[3], but the corresponding thin-film properties of their ground-state structures remain largely unknown. An additional reason to examine thin-film synthesis pathways to stable materials with layered 2D-like structures is that they tend to host unusual semiconductor or quantum properties promising for practical applications[4]. Among nitrides, examples include high mobility in 2D-layered hexagonal boron nitride (hBN)[5], 2D electron gas at GaN/AlGaN interfaces[6] and diverse properties of nitrogen-containing intermetallic MAX phases[7,8].

Many known nitrides are thermodynamically stable in layered, 2D-like crystal structures[9], such as $ScTaN_2$ (refs. 10,11), $MgTa_2N_3$ (refs. 12,13) and $BaZrN_2$ (refs. 14,15). These materials belong to a layered family of multivalent ternary nitrides that combines two metal cations with a nitrogen anion in equal amounts and with charge-balanced stoichiometry[16]. These layered 2D-like materials feature alternating sheets of MN_x polyhedra (where M is a metal and $x = 4–10$), such as octahedra, tetrahedra, square pyramids and trigonal prisms, and are distinct from 3D wurtzites[17], 3D rocksalts[18] or 3D perovskites[19] formed by elemental layering[20]. Several multivalent ternary nitrides with 1–1–2 stoichiometry ($FeWN_2$, $MnMoN_2$ (ref. 21), $CoMoN_2$ (ref. 22)) and 1–2–3 stoichiometry ($MgTa_2N_3$ (ref. 12), $MgNb_2N_3$) have been synthesized as layered structures by bulk methods[23,24], and others ($ZnZrN_2$ (ref. 25), $ZnMoN_2$ (ref. 26), $MgWN_2$ (ref. 27)) have been calculated to be stable in 2D-layered structures.

Some layered 2D-like nitride materials are theoretically predicted to have unique properties, such as tunable topological and Dirac semimetal states in $MgTa_2N_3$-based alloys[28,29]. Unfortunately, their electrical transport and optoelectronic properties remain experimentally

[1]National Renewable Energy Laboratory, Golden, CO, USA. [2]Colorado School of Mines, Golden, CO, USA. [3]National Institute of Standards and Technology, Gaithersburg, MD, USA. [4]Argonne National Laboratory, Lemont, IL, USA. ✉e-mail: andriy.zakutayev@nrel.gov

https://doi.org/10.1038/s44160-024-00643-0

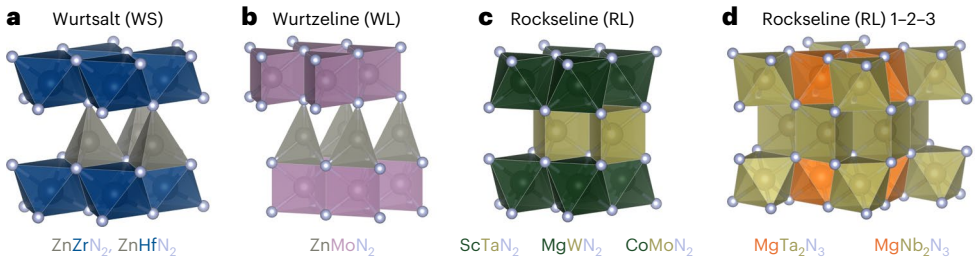

Fig. 1 | Examples of layered, 2D-like crystal structures among multivalent ternary nitrides. a, Wurtsalt (WS) structure consisting of alternating sheets of tetrahedra and octahedra. **b**, Wurtzeline (WL) structure consisting of alternating sheets of tetrahedra and trigonal prisms. **c**, Rockseline (RL) structure with 1–1–2 stoichiometry consisting of alternating sheets of edge-sharing octahedra and edge-sharing trigonal prisms. **d**, RL structure with 1–2–3 stoichiometry.

unknown: these properties are difficult to measure for polycrystalline powders, and single crystals are even more challenging to grow in nitride chemistry. Thin films suitable for property measurements are commonly synthesized by rapid quenching from vapour or plasma to solid phase at a rate of up to 10^{10} K s^{-1} (ref. 30). This synthesis pathway leads to metastable polymorphs with isotropic 3D bonding and very different properties compared to the thermodynamically stable 2D-layered structures[16]. For instance, a layered 2D-like ground state of $MgWN_2$ is predicted to be a semiconductor, whereas a 3D metastable polymorph of $MgWN_2$ is predicted to be a metal[27]. It remains unclear both (1) why thin-film synthesis favours metastable 3D structures, and (2) how to reliably achieve nitrides with layered 2D-like structures in film form.

Here we describe a synthesis pathway to nitride thin films with stable layered 2D-like crystal structures through a 3D long-range disordered metastable intermediate structure. Although growth on heated substrates results in decomposition above 600 °C in vacuum, the $MgMoN_2$ with a stable layered 2D-like cation-ordered rockseline structure forms after 700–1,100 °C annealing of a 3D metastable intermediate rocksalt structure deposited at ambient temperature. The emergence of this cation-ordered layered 2D-like product may seem surprising because the 3D isotropic intermediate structure is apparently cation-disordered according to X-ray diffraction (XRD), despite the difference in magnesium and molybdenum atomic properties. Experimental and theoretical pair distribution function (PDF) analysis reveals a layered short-range order in the rocksalt (RS) structure that is reminiscent of the polyhedral layering within the rockseline (RL) structure. We theoretically identify a simple displacive transformation pathway from a 3D RS intermediate to a layered 2D-like RL product, and experimentally quantify a 100 meV per atom transformation barrier consistent with the calculations. These $MgMoN_2$ results give insight into synthesis of layered 2D-like products, and are extended here to $ScTaN_2$, $MgWN_2$ and $MgTa_2N_3$, which may aid the synthesis of many other layered materials in thin-film form.

Results and discussion

Experimental discovery of rocksalt-to-rockseline transition

Crystal structures of layered 2D-like multivalent ternary nitride materials are most easily described as a mixture of the 3D structure archetypes that embody each layer (Fig. 1). For example, $ZnZrN_2$ and $ZnHfN_2$ are predicted to form in thermodynamically stable layered 2D-like 'wurtsalt' (wurtzite–rocksalt (WS); Fig. 1a) structure[31], but thin-film synthesis of $ZnZrN_2$ up to 300 °C results in metastable 3D RS or hBN crystal structures[25]. Similarly, the Zn_3MoN_4–$ZnMoN_2$ family crystallizes in a 3D wurtzite structure across the entire chemical composition range, instead of crystallizing in the thermodynamically stable layered 2D-like 'wurtzeline' (wurtzite–nickeline (WL); Fig. 1b) structure at $ZnMoN_2$ composition[26]. Recently, $MgWN_2$ thin-film synthesis on a heated substrate also resulted in two metastable 3D RS and hBN structures, whereas the stable layered 2D-like 'rockseline' (rocksalt–nickeline (RL); Fig. 1c) structure with 1–1–2 stoichiometry was synthesized by bulk ceramic methods[27], and rockseline structures with 1–2–3 stoichiometries have been also reported for $MgTa_2N_3$ (ref. 12) (Fig. 1d). Growing these zinc- and magnesium-based ternary thin films on substrates held at higher temperatures to achieve the ground-state layered structure was not feasible, probably due to re-evaporation of ZnN_x- and MgN_x-based components caused by their high vapour pressure.

To experimentally realize $MgMoN_2$ with a layered 2D-like crystal structure, thin films of Mg–Mo–N were synthesized by radiofrequency co-sputtering from metallic magnesium and molybdenum precursors in an argon/nitrogen atmosphere, and then subjected to rapid thermal annealing under atmospheric nitrogen pressure. The results of composition measurements indicate that the synthesized $MgMoN_2$ materials in the Mg/(Mg + Mo) = 0.50–0.75 range (as measured by X-ray fluorescence (XRF)) are free of oxygen impurities (Fig. 2a and Supplementary Fig. 1a). According to the XRD results, the as-deposited Mg–Mo–N films form in a nanocrystalline RS-derived crystal structure with mixed magnesium and molybdenum occupancy of the cation lattice across a broad range of studied compositions (Mg/(Mg + Mo) = 0.20–0.95) and temperatures (Fig. 2b). LeBail fits of the RS lattice constants as a function of cation composition in the as-deposited samples measured by synchrotron grazing-incidence XRD show the expected linear trend (Fig. 2c).

After annealing for 3 min at T_{ann} = 800–1,100 °C, the crystal structure transforms from RS to RL (Fig. 2c,d), with phase-pure RL material obtained in the Mg/(Mg + Mo) = 0.45–0.70 range. This layered phase cannot be achieved by deposition on the substrate heated to 800 °C under low sputtering pressure because even at 600 °C, there is very little magnesium incorporation in the growing film due to the high MgN_x vapour pressure (Supplementary Fig. 2a), similar to $MgWN_2$ (ref. 27) and ZnN_x in $ZnZrN_2$ (ref. 25). Outside of the Mg/(Mg + Mo) = 0.45–0.70 composition window, the RS structure persists after annealing. However, when annealing above 1,100 °C (Fig. 2b) and for longer than 3 min (Supplementary Fig. 1b) a reaction of molybdenum with the silicon substrate is observed, as indicated by the Mo_3Si diffraction peaks.

The results of synchrotron grazing-incidence wide-angle X-ray scattering (GIWAXS) measurements for $MgMoN_2$ films annealed at 600 °C (RS phase) and 900 °C (RL phase) are shown in Fig. 2d alongside the two crystal structure models. All RS and RL peaks expected from reference patterns are clearly resolved, with some deviation in the peak intensity due to preferential orientation effects or Mg/Mo cation disorder across O_h/T_p sites. GIWAXS patterns for the Mg_3MoN_4 composition with the RS structure are shown in Supplementary Fig. 2b. The measured RL-$MgMoN_2$ data show a strong low-angle (002) and subsequent (00L) peaks indicative of some degree of magnesium and molybdenum ordering on the O_h and T_p sites in the RL structure, whereas the measured RS-$MgMoN_2$ data do not show any peaks related to this long-range cation ordering. It is surprising that the apparently cation-disordered RS structure transitions into a clearly cation-ordered RL structure during the annealing process, and that the metastable

https://doi.org/10.1038/s44160-024-00643-0

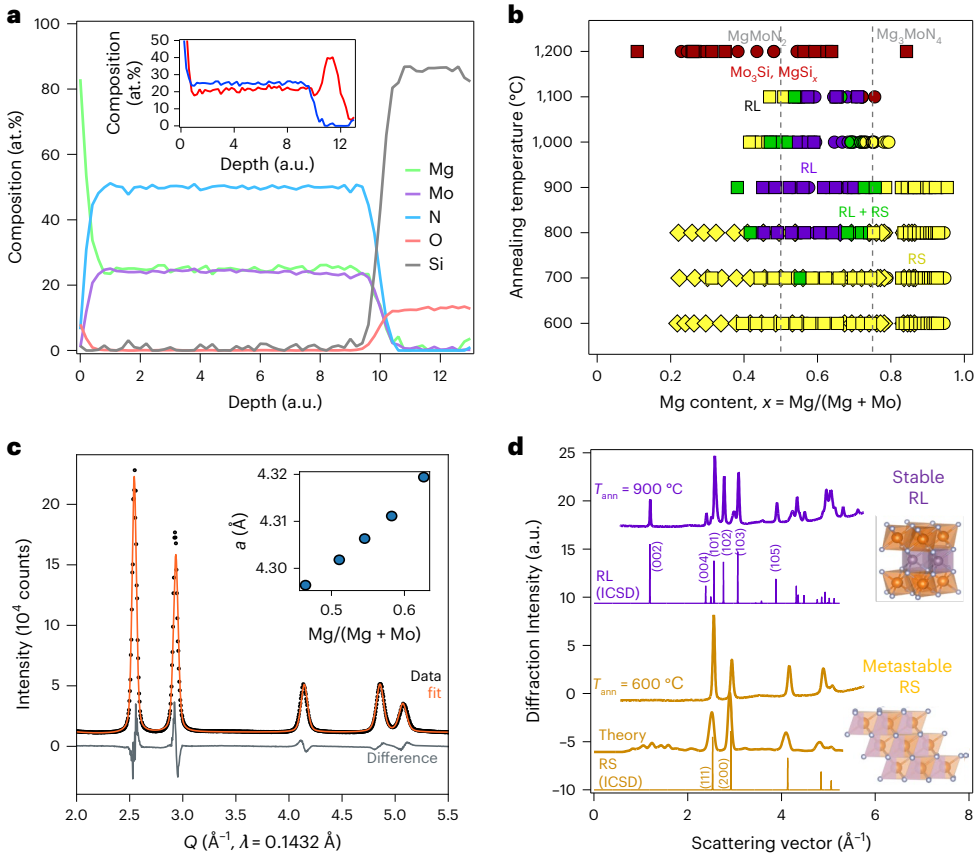

Fig. 2 | Chemical composition and crystal structure of $MgMoN_2$. **a**, Composition measurements as a function of depth, showing a negligible amount of oxygen and some magnesium accumulation at the substrate interface after annealing (inset). **b**, Growth map showing formation of the layered 2D-like RL phase at $MgMoN_2$ and Mg-rich compositions above 700 °C. **c**, LeBail fit performed on synchrotron grazing-incidence XRD in the RS structure for as-deposited films, and the relationship between lattice parameter *a* and cation ratio (inset). **d**, Synchrotron GIWAXS data and crystal structures of $MgMoN_2$ in metastable 3D RS and stable layered 2D-like RL phases, along with two theoretical reference patterns from the Inorganic Crystal Structure Database (ICSD), and one computationally simulated average disordered RS pattern.

3D RS structure forms in the first place instead of the stable layered 2D-like RL structure.

Theoretical explanation of metastable rocksalt synthesis

From a theoretical point of view, the experimental realizability of various crystalline phases is related to the size of the corresponding local minima on the potential energy surface. The size of a local minimum—the total volume occupied by its attraction basin in the configuration space of atoms—measures the probability of a structure falling into that minimum. Hence, a larger basin of attraction implies higher chances for its experimental realization. As was shown previously, this principle explains all experimentally observed metastable polymorphs in several elemental or binary chemistries, such as elemental silicon[32], binary oxides[33] and group IV carbides[34], and the emergence of the disordered RS phase in the thin-film synthesis of $ZnZrN_2$ in lieu of the ordered 'wurtsalt' ground state[25].

To explain the $MgMoN_2$ experimental results described above, we investigated relevant features of the potential energy surface (PES) of $MgMoN_2$ using first-principles structure sampling[33]. This involved generating 5,000 random structures, relaxing them to the closest local minimum, and classifying them into groups with the same underlying structure type (Methods). As shown in Fig. 3a, the tallest peak in the space-group-resolved thermodynamic density of states (TDOS) with 314 members has the RS-type parent structure with space group (s.g.) 225 (*Fm*−3*m*), with the relatively narrow energy range of 0.5–1.5 eV per formula unit due to the variations in the Mg/Mo site occupancies, as observed in entropy-stabilized ceramics. There are two other relatively populous six-fold coordinated hexagonal structures (s.g. 160 and s.g. 166) with 10×–50× smaller representation than RS, made of edge- and face-sharing octahedra (s.g. 166) or a combination of octahedra and trigonal prisms (s.g. 160), which can be viewed as a disordered version of the ground state s.g. 194 (shown as a dashed line in Fig. 3a). The low-symmetry structure types (s.g. 1 and s.g. 2) have high energy and large spread, and are therefore important for description of the amorphous or glassy state[35].

Supplementary Fig. 3a shows the temperature dependence of the configurational free energies of all structure types determined by structure sampling[23]. Our calculations include the RL phase, which is represented by the dashed line and is assumed to have no configurational entropy (occurrence of 1). The RS phase of $MgMoN_2$ has the highest entropy because of its large and narrow TDOS, and it becomes the structure with the lowest free energy for temperatures above 2,000 K (Supplementary Fig. 3b). The films deposited at ambient conditions exhibit a cation-disordered RS structure that was predicted above 2,000 K, because their kinetically frozen cation disorder corresponds to this effective temperature. It has been shown that equilibrium calculations for temperatures of 1,000–2,500 K reproduce the cation disorder that exists in materials grown in thin-film form under non-equilibrium conditions, such as $ZnZrN_2$ (ref. 25), Co_2ZnO_4 and Co_2NiO_4 (ref. 36).

The RL phase known from bulk synthesis of $MgMoN_2$ (s.g. 194)[23,24] did not occur at all in the random structure sampling, indicating that the stable layered RL structure of $MgMoN_2$ has a very narrow local minimum on the PES. This is a markedly different result than for $ZnZrN_2$

https://doi.org/10.1038/s44160-024-00643-0

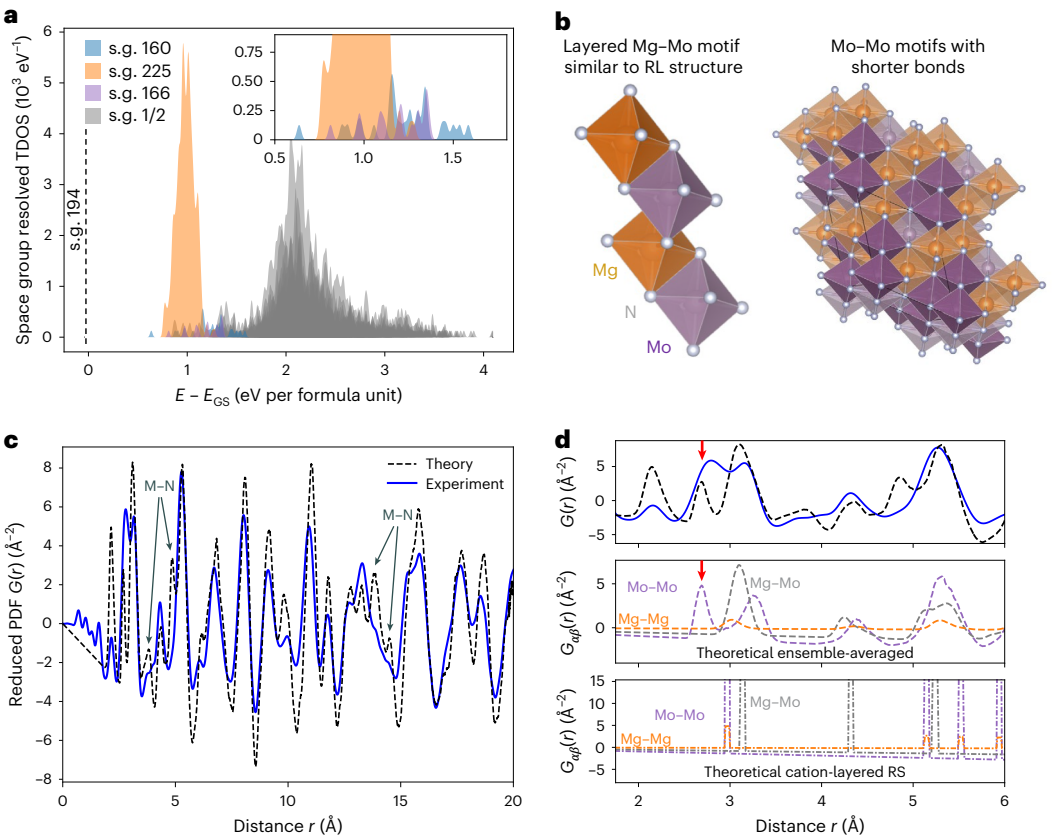

Fig. 3 | Local short-range atomic order in metastable RS-$MgMoN_2$. a, Space-group-resolved TDOS of $MgMoN_2$, showing the prevalence of the RS structure s.g. 225. **b**, The cation-layered -Mg-Mo-Mg-Mo RS motif along the (111) axis (left), taken from a RS structure predicted by structure sampling (right), with shortened Mo–Mo distances (2.62 Å, 2.75 Å, 2.72 Å) in the highlighted MoN_6 octahedra. **c**, Measured reduced PDF $G(r)$ of as-deposited $MgMoN_2$ films (blue line) and theoretical model from structure sampling (dashed black line), showing good agreement. **d**, Magnified comparison of experimental and theoretical PDF in the low-r region (top), with a red arrow indicating the 2.7 Å peak that does not exist in the cation-disordered RS model (bottom), but results from Mo–Mo interactions (middle).

and for all other systems we investigated, for which the ground-state structures are consistently found by structure sampling. However, atomic motifs having a -Mg-Mo-Mg-Mo- cation ordering, referred to as the 'cation-layered RS motif', were identified within all RS-type structures from the structure sampling (Fig. 3b). In these motifs, Mo(1) is in the [110] crystallographic direction from Mg(1), Mg(2) is in the [101] direction from Mo(1), and Mo(2) is in the [110] crystallographic direction from Mg(2). Periodic boundary conditions applied to this motif result in a (111) superlattice with alternating magnesium and molybdenum layers.

It would be statistically probable to find this four-atom -Mg-Mo-Mg-Mo- motif even in a fully random alloy because the probability of finding a single sequence of four atoms occupied in a certain way is $(1/2)^4$. Moreover, given the relatively large number of ways a given motif can be constructed, a large fraction of cations can be expected to be a part of at least one such motif. Therefore, we hypothesize that the long-range-ordered RL phase is experimentally realized (Fig. 2) by a facile structural transformation from the short-range-ordered RS phase (Fig. 3b). For this to happen at the relatively low annealing temperature of 700 °C, the experimental RS structure should contain domains where the local arrangement of magnesium and molybdenum atoms provides a seed for alternating (111) layers, similar to the alternating (001) planes of the RL product.

Local structure from theoretical and experimental PDF

The short-range cation order in the long-range-disordered RS intermediate structure was measured using synchrotron grazing-incidence PDF analysis of a series of preannealed thicker (600–800 nm) $MgMoN_2$ samples, with the quartz substrate contribution measured and subtracted. The results of composition-dependent XRD measurements and LeBail fits (Supplementary Fig. 4b) are consistent with the lattice constant linearly increasing as a function of the magnesium content (Fig. 2c). The measured PDF was fitted using a randomly disordered RS model across a wide r range (2–30 Å; Supplementary Fig. 4a). Although the high-r range (>10 Å) matched this model well, a surprising difference was observed in the short-distance local ordering range (2–7 Å) in which the PDF fit residuals are high, especially in the 2.5–3.0 Å region. This implies that the length scale of the short-range correlations is of the order of 5 Å, which would be invisible to traditional long-range XRD measurements. The lowest-r (<2 Å) oscillations of the experimental data are due to truncated Fourier transform effects and substrate correction.

To understand the difference(s) between the experimentally measured PDF and the disordered rocksalt PDF model in the 2.0–3.0 Å region, a theoretical PDF was obtained through ensemble averaging over all RS-type structures (Fig. 3a). The positions of peaks in the experimental data are well matched by the theoretical model across the entire r region (Fig. 3c), including the 2–3 Å range (Fig. 3d, top panel). Figure 3d (middle and bottom panels) shows the contributions of specific atom type pairs to the PDF (denoted as the partial PDF). In the cation-layered RS structure, the nearest-neighbour Mo–Mo and Mg–Mg partial peaks are superimposed at the same distance r = 3.1 Å (Fig. 3d, bottom). In the ensemble-averaged theoretical PDF of the disordered RS model (Fig. 3d, middle), the Mg–Mo and the Mg–Mg partial peaks are also present at similar distances (r = 2.95 Å). However the

https://doi.org/10.1038/s44160-024-00643-0

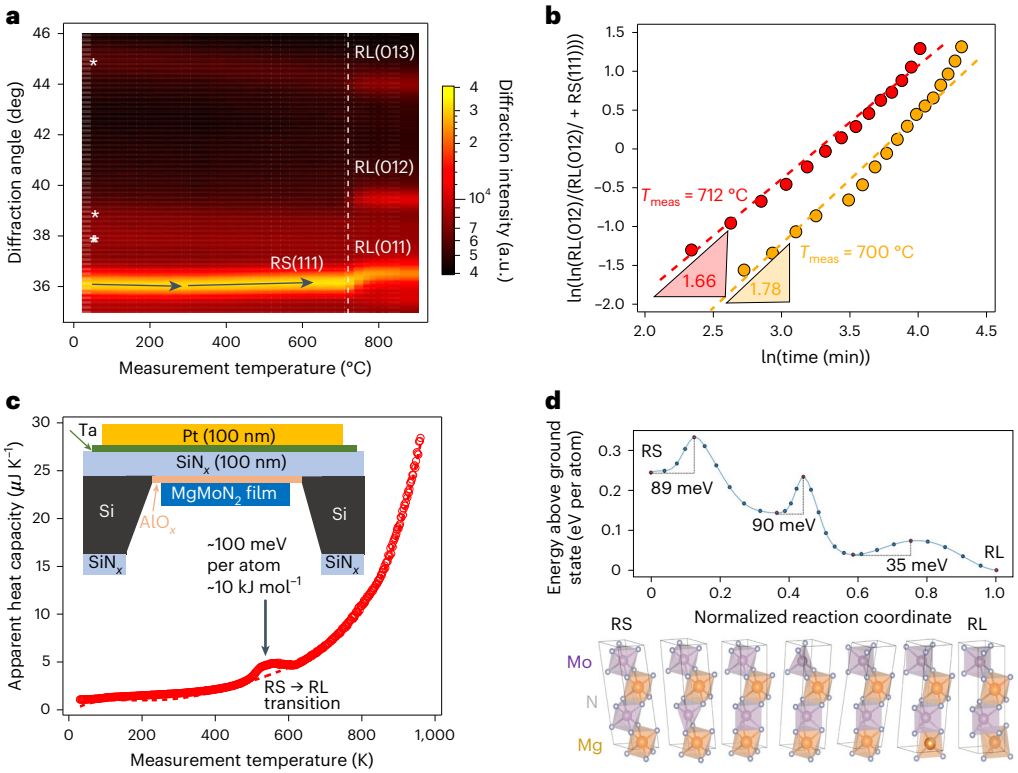

Fig. 4 | In situ measurements of the $MgMoN_2$ RS–RL phase transformation. **a**, Temperature-dependent XRD showing negative thermal expansion of the RS phase in the 300–600 °C range and a sharp transition to the RL phase around 700 °C. Asterisks indicate broad peaks from a polymeric sample cover dome. **b**, Analysis of these time-dependent measurements at 700 °C and 712 °C, resulting in a slope of $n = 1.7$, which reflects the combination of instantaneous 2D nucleation ($n = 1.5$) and 3D diffusion ($n = 2.0$). **c**, Nanocalorimetry results using a measurement chip (inset), showing a small endothermic signal associated with overcoming the RS–RL energy barrier. **d**, The energy profile (top) and the corresponding structure (bottom) for the transformation of the layered RS structure to the RL structure (continuous line), as calculated using a solid-state nudged elastic band (discrete symbols), with red symbols indicating the critical steps of the pathway (see text).

Mo–Mo partial is split into two peaks: a peak blending with the Mg–Mo peak at $r = 3.2$ Å, and most importantly another peak around $r = 2.7$ Å, also known in other layered ternary transition metal nitrides[10]. We identify that this splitting arises from the relaxations of the molybdenum atoms towards shorter distances that occur in disordered RS-type structures (Fig. 3d, middle).

The modelled Mo–Mo peak (Fig. 3d, middle) explains the measured PDF peak at approximately $r = 2.0$–3.0 Å (Fig. 3d, top) that is not captured by cation-layered (Fig. 3d, bottom) cation-disordered (Supplementary Fig. 4a) RS models. It is unlikely that this measured peak is due to Mo–Mo distances in the metallic body-centred cubic molybdenum structure because its intensity scales with magnesium content (Supplementary Fig. 4b) and because the single-phase RS XRD LeBail fit residuals are low (Supplementary Fig. 3b). The overall agreement between experimental and theoretical PDFs (Fig. 3c), and especially the agreement for the distinct Mo–Mo peak in the 2.5–3.0 Å range, are evidence for the similarity between the as-grown $MgMoN_2$ thin films and the ensemble average of RS-type structure samples (Fig. 3a), but not the RS model with random cation disorder (Supplementary Fig. 4a). Due to this direct correspondence, the cation-layered -Mg-Mo-Mg- motif found in the RS-type sample structures (Fig. 3b) is theorized to be found also in the as-grown $MgMoN_2$ thin films. For this cation-layered RS motif (Fig. 3b) to transform into the site-layered RL structure, the kinetic barrier between these two phases should be low.

Measurements and calculations of the transformation pathway

To characterize the RS-to-RL crystallographic transformation process, we performed temperature-dependent XRD measurements on select samples at the $MgMoN_2$ composition. The XRD colour intensity map as a function of measurement temperature (Fig. 4a) shows a sharp transition around 700–720 °C, suggesting a facile transformation pathway between the RS and RL structures. The unusual negative thermal expansion of the RS lattice in the 300–600 °C range (Supplementary Fig. 5) should also be noted. Time-dependent XRD measurements at two different temperatures in this range show a gradual increase of the RS (111) peak intensity and a decrease of the RL (012) peak intensity (Supplementary Fig. 6). Fitting the XRD data measured at 700 °C and 712 °C to a sigmoidal Avrami equation[37] in both cases leads to an exponent value of approximately $n = 1.7$ (Fig. 4b). The measured $n = 1.7$ exponent could correspond to a combination of 2D interface-controlled growth ($n_g = 2$) that could be rationalized by the 2D thin-film geometry, and a 3D diffusion-controlled growth ($n_g = 1.5$) that could be rationalized by the observation of long-range Mg–Mo atom diffusion (Fig. 2a)

To measure the energy scale of the phase transformation process, we performed nanocalorimetry measurements in ultrahigh-purity N_2 (ref. 38) for 100 nm thin $MgMoN_2$ films deposited on microfabricated silicon chips. The apparent heat capacity as a function of measurement temperature (Fig. 4c) shows an endothermic signal that is 25 °C in width and has an integrated energy value of approximately 10 kJ mol^{-1} (100 meV per atom). It is not entirely clear why this endotherm appears at 550–600 °C instead of at 700 °C, the temperature at which the phase transformation is observed by both ex situ XRD (Fig. 2) and in situ XRD (Fig. 4a), with possible temperature measurement error accounting for 25–75 °C. Possible physical reasons include (1) the need for growth of the locally transformed nuclei to be observed by extended crystal structure measurement methods, and (2) the strong dependence of the phase-transformation process on the heating rate (0.1–10 K s^{-1}

https://doi.org/10.1038/s44160-024-00643-0

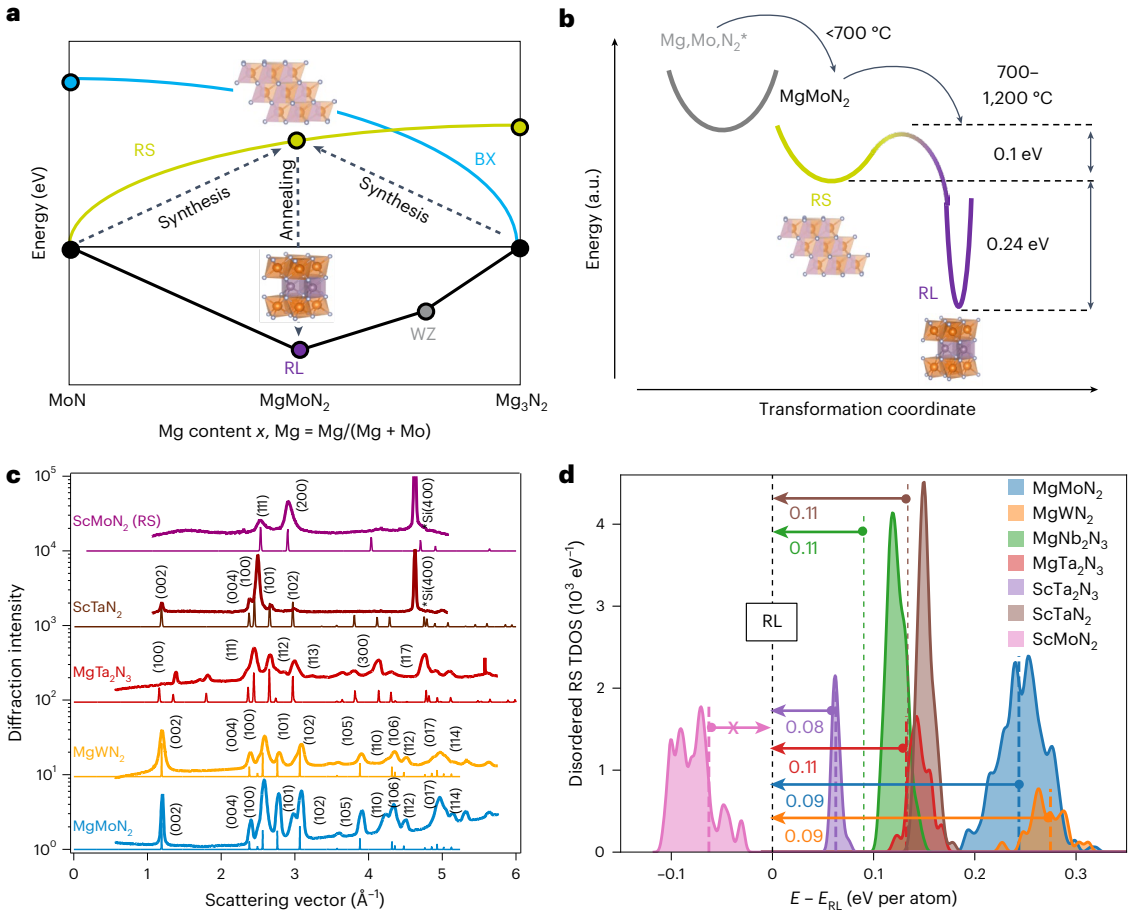

Fig. 5 | 3D-to-2D synthesis pathway for $MgMoN_2$ and extension to other materials chemistries. a, Convex hull diagram, showing co-deposition of a high-energy 3D RS-$MgMoN_2$ intermediate (yellow) and its crystallographic transformation to the layered 2D-like RL product (purple), with BX (blue) indicating the competing bixbyite structure of Mg_3N_2. **b**, Potential energy landscape at a fixed $MgMoN_2$ composition, showing a low-energy 0.1 eV barrier between the broad metastable 3D RS energy valley (yellow) and a stable deep, narrow 2D-like RL energy well (purple). **c**, Experimentally measured synchrotron GIWAXS patterns of four layered 2D-like RL thin-film nitride materials, $MgMoN_2$, $MgWN_2$, $MgTa_2N_3$ and $ScTaN_2$, and one 3D RS, $ScMoN_2$, including their minimal RS-to-RL annealing temperatures. **d**, Calculated TDOS and transformation energy barriers from the cation-layered RS to structurally layered RL, indicating that all of the materials except $ScMoN_2$ should transition from the RS to the RL structure.

for XRD versus 10^3–10^4 K s^{-1} for nanocalorimetry). Nevertheless, the precise measurement of the small 100 meV per atom calorimetry signal for a 100 nm nitride thin film is indicative of the phase-transformation process having a relatively low kinetic barrier.

To calculate the energy barrier, we modelled the transformation pathway from the cation-ordered RS structure (α-$NaFeO_2$-type) to the cation-ordered 2D-like RL structure[39]. The calculated barrier of approximately 90 meV per atom (Fig. 4d) is consistent with the experimental observation that the transition occurs at approximately 600–700 °C, and the apparent change in heat capacity during that transition, suggesting that small domains of the cation-layered RS motif are present in the thin film. The first step of this pathway involves the transformation of layers of MoN_6 octahedra to MoN_6 trigonal prisms and is characterized by the relative shift of a layer of nitrogen atoms: one Mo–N bond per molybdenum atom is broken and then reformed in this process (89–90 meV per atom). In the second step, the layers of MgN_6 octahedra must invert: one magnesium atom per two formula units must move in every other layer, where two Mg–N bonds per magnesium atom are broken (35 meV per atom). The barrier is not expected to change with the introduction of cation disorder into the material, as shown for the barriers in supercells with the magnesium and molybdenum sites swapped (Supplementary Fig. 7), although the 90 meV per atom rate-limiting step switched from the first to the second one.

Discussion of rockseline $MgMoN_2$ crystallization mechanisms

In this work, we experimentally discovered (Figs. 2 and 4) and theoretically explained (Figs. 3 and 4) a synthesis pathway to nitride thin films with layered 2D-like crystal structures (Fig. 1) from 3D atomically mixed intermediates deposited from vapour precursors. The key insights are that:

(1) The 3D structures are high-probability metastable phases favoured by kinetically limited growth methods (Figs. 2 and 3), whereas stable layered 2D-like structures have a low probability of formation.
(2) A layered 2D-like crystal structure can form by facile atomic transformation (Fig. 4) from a 3D intermediate that has no long-range cation order but features layered cation-ordered local motifs (Fig. 3).
(3) These motifs (Fig. 3) serve as nucleation centres for this crystallographic transformation into a long-range-ordered 2D-like structure experimentally achieved by annealing (Figs. 2 and 4).

This synthetic pathway is supported by a direct comparison of the measured and calculated PDFs (Fig. 3) and the energy barrier (Fig. 4) between the 3D intermediate and the 2D-like product.

A schematic representation of the synthetic pathway on an energy scale in the Mg–Mo–N compositional coordinates is shown in Fig. 5a. The first step of the process is the formation of a high-energy,

long-range-disordered but short-range-ordered RS-$MgMoN_2$ 3D crystal structure from vapour-phase magnesium, molybdenum and nitrogen precursors (Fig. 5a). The second step is transformation of this 3D metastable intermediate structure into a stable layered 2D-like RL-$MgMoN_2$ structure with both short-range and long-range cation order (Fig. 5a). Figure 5b illustrates the potential energy surface at a fixed $MgMoN_2$ composition in energy versus configurational space coordinates. The potential well corresponding to the ground-state layered RL-$MgMoN_2$ structure is deep and narrow. However, it is separated by a small 100 meV potential energy barrier from a much wider—and hence much more probable—3D RS-$MgMoN_2$ well (Fig. 5b) that is slightly higher in energy. This small potential barrier corresponds to the facile RS–RL local transformation pathway identified in Fig. 4.

The synthetic pathway reported here is not limited to thin-film synthesis methods; it should also apply to bulk synthesis approaches in which intimate atomic intermixing is involved. For example, in the case of $MgMoN_2$ synthesized in bulk by a metathesis reaction, an intermediate 300–450 °C heating step to promote Mg–M–N bond formation, followed by 800–900 °C annealing of these intermediates, successfully resulted in the layered 2D-like RL-$MgMoN_2$ structure. In contrast, direct heating to the 800–900 °C reaction temperature results in formation of a 3D RS structure, probably accompanied by volatilization of Mg–N (ref. 40). Bulk syntheses of $MgMoN_2$ (ref. 23) and $MgWN_2$ (ref. 27) by a conventional one-step route require a much higher temperature (1,100 °C) and result in residual tungsten or molybdenum and other impurities. In the case of $ScTaN_2$ bulk powders, heating to 1,546 °C for 200 h was required to obtain a phase-pure product[10], illustrating the advantage of the facile transformation pathway for synthesis of layered ternary nitrides reported here.

Extension to other layered multivalent ternary materials

To demonstrate the universality of the synthesis pathway discovered in this work for RL-$MgMoN_2$, we attempted synthesis of five other materials with alternating layers of magnesium or scandium in O_h coordination, and molybdenum, tungsten or tantalum in T_p coordination. These ternary nitride materials include $MgWN_2$ (ref. 27), $MgTa_2N_3$ (ref. 13) and $ScTaN_2$ (ref. 10), which have been reported to have a layered 2D-like crystal structure based on bulk synthesis, and $MgNb_2N_3$ and $ScMoN_2$, which have not been reported in the Inorganic Crystal Structure Database. Thin films of these materials deposited at ambient temperature crystallize in a 3D disordered RS structure. The $MgWN_2$, $MgTa_2N_3$, $MgMoN_2$ and $ScTaN_2$ annealed at 800–1,200 °C (Fig. 5c) transform into layered 2D-like structures with cation ordering indicated by characteristic low-angle diffraction peaks. However, $ScMoN_2$ could not be synthesized in the RL structure (Fig. 5c), and the $MgNb_2N_3$ synthesis results were inconclusive (Fig. S8).

Figure 5d shows the structure sampling (2,000 structures) and kinetic barrier modelling results for seven ternary nitrides, namely, $MgWN_2$, $MgTa_2N_3$, $ScTaN_2$, $MgNb_2N_3$, $ScTa_2N_3$, $ScMoN_2$ and $MgMoN_2$, in comparison with total energy calculations for the RL structure (calculated for all prototypical structures from Fig. 1). The frequency of RS occurrence far exceeds any other structure type (Supplementary Fig. 9), and a high percentage of atoms participate in the RS layered motifs (Supplementary Table 1). The calculated barriers for the structural transformation from the ordered RS into the ordered RL phase are all in the 0.08–0.11 eV per atom range (Supplementary Fig. 10). These barriers correlate well with the annealing temperatures needed for the realization of a RL phase (Supplementary Fig. 11). For all the investigated nitrides the RL structure has the lowest energy, with exception of $ScMoN_2$, indicating that the transformation from the RS structure is unlikely. This theoretical result can be explained by the O_h rather than T_p coordination preference of the Mo(III) ion with d^3 electronic configuration[41], and is consistent with the experimental observation (Fig. 5c), providing a false-negative validation of our theoretical method.

The successful synthesis of $MgWN_2$, $MgTa_2N_3$, $MgMoN_2$ and $ScTaN_2$ layered nitride materials in thin-film form (Fig. 5c), and the theoretical explanation of their realization (Fig. 5d), support the generality of the transformation pathway described in this paper. These results are also interesting because the thermoelectric[11] and quantum[28,29] properties of these RL materials were predicted by theoretical calculations but have not yet been measured due to difficulties with performing thin-film synthesis. The general synthesis pathway demonstrated in this work for layered RL structure may also apply to nitrides with $KCoO_2$-type structures such as $SrTiN_2$ and $BaZrN_2$ (Supplementary Fig. 12), with two distinct coordination environments that have recently attracted renewed attention due to their electronic properties[42,43]. This pathway may also apply other site-layered ternary nitrides, but probably not to cation-layered single-site wurtzite[17] or rocksalt[18] phases. It would also be interesting to perform similar calculations and experiments for the layered nitride and carbide MAX phases[8], of which only 4–6 out of >160 materials have been grown in thin-film form[7].

Conclusions

We synthesized $MgMoN_2$ with a stable layered 2D-like crystal structure from a 3D disordered metastable intermediate, and quantified the 3D-to-2D transformation pathway by in situ measurements and theoretical calculations. As-deposited $MgMoN_2$ thin films crystallize in an apparently cation-disordered RS structure with 3D octahedral coordination, and rapidly transform into a cation-ordered layered 2D-like RL structure above 700 °C. Experimental PDF measurements show peak splitting around 2.7 A, supporting the computational model of a short-range-ordered 3D RS structure. The calculated transformation pathway has a 100 meV per atom energy barrier measured using nanocalorimetry, further validating the 3D-to-2D transformation model. This $MgMoN_2$ discovery means that other metastable 3D nitride materials may have short-range order and a transformation pathway into stable, layered 2D-like crystal structures, such as $MgWN_2$, $MgTa_2N_3$ and $ScTaN_2$ shown here. These results also imply that it should be possible to control the long-range order of the final layered product by altering the short-range order of the intermediate during the synthesis, which is important for fine-tuning quantum and semiconducting properties of these materials.

Methods

Experimental

We synthesized thin films (typically 150–300 nm thick) of Mg–Mo–N by radiofrequency co-sputtering from metallic magnesium and molybdenum precursors in an argon and nitrogen atmosphere onto silicon substrates without (80 °C) and with (<600 °C) intentional heating, and subjected them to rapid thermal annealing in flowing nitrogen at 600–1,200 °C for 3–30 min. Metal composition was quantified with XRF, and anion composition was measured with Auger electron spectroscopy (AES). The crystal structure determined from laboratory and synchrotron XRD was measured as a function of the Mg–Mo–N chemical composition and at various deposition and annealing temperatures.

Multiple Mg–Mo–N thin-film sample libraries with different Mg/Mo composition gradients were deposited by radiofrequency co-sputtering on to ambient-temperature (60–80 °C due to unintentional heating) commercial silicon substrates, some with a chemical vapour deposition-grown SiN_x layer, from 2 inch (50 mm) diameter magnesium and molybdenum targets held at 30–60 W power. Typical depositions were performed in a mixture of flowing Ar/N_2 (6/3 sccm) in a total of 6 mtorr (8×10^{-6} atm) pressure in a vacuum chamber with 10^{-7} torr (1.3×10^{-9} atm) base pressure for 60–120 min, resulting in 150–300 nm thin films. Thinner samples deposited for 15–30 min on Si/SiN_x membrane substrates, and thicker samples deposited for 4–6 h on quartz, were deposited for nanocalorimetry and PDF measurements, respectively. Some samples had a 50 nm thin SiN_x or AlN capping layer deposited on the top of the film to prevent surface oxidation

during storage. The synthesized samples were treated by rapid thermal annealing (ULVAC MILA-5000 series) in the 600–1,200 °C temperature range for 3–30 min with a 1 min temperature ramp up and a 2–5 min temperature quench in flowing nitrogen.

The cation composition of the Mg–Mo–N films was measured using XRF (Bruker M4 Tornado) and quantified using XMethods software with a manual conversion from wt% to at.%. The anion composition and unintentional oxygen content (if any) was determined from AES measurements using standard sensitivity factors for oxygen and nitrogen, with magnesium and molybdenum compositions calibrated to those of the XRF values. Nanocalorimetry measurements were performed on as-deposited Mg–Mo–N films in a nitrogen atmosphere, with an average heating rate of ~10,000 °C s^{-1}. The nanocalorimeter sensor (Fig. 4c inset) includes a platinum thin-film heater deposited over a SiN_x membrane which is suspended over a silicon frame. The platinum heater also functions as a temperature sensor based on the temperature coefficient of the resistance of platinum through calibration using the melting point of aluminium. A 10 nm alumina barrier was deposited between the sensor and sample using atomic layer deposition to prevent any potential reaction between the sample and the SiN_x.

Laboratory XRD patterns were collected on a Bruker D8 Discover using Cu Kα radiation and equipped with a 2D detector, and analysed with CombIgor software[44] with data stored in the National Renewable Energy Laboratory's HTEM database[45]. In situ laboratory XRD measurements were performed on a resistively heated stage in a polymer dome under flowing nitrogen. To study the kinetic mechanism nucleation and growth during this phase-transformation process, we analysed the time-dependent XRD data using the sigmoidal Avrami equation from the Johnson–Mehl–Avrami–Kolmogorov model[37], $I(t) = 1 - \exp(-kt^n)$, where I is the measured XRD intensity, $n = n_n + n_g$ are the nucleation and growth components of the Avrami exponent, and k is a constant. Given the characteristically sharp temperature dependence (Fig. 4a), we assume an instantaneous heterogeneous nucleation process ($n_n = 0$). This model is commonly used to describe isothermal nucleation of growth kinetics in different areas of materials science, for example, polarization domains in ferroelectric materials, most recently nitrides[46].

High-resolution synchrotron grazing-incidence wide-angle X-ray scattering (GIWAXS) measurements were performed at beamline 11-3 at the Stanford Synchrotron Radiation Lightsource (SSRL), SLAC National Accelerator Laboratory. The data were collected with a Rayonix 225 area detector at room temperature using a wavelength of λ = 0.9744 Å, a 1° or 3° incident angle, a 150 mm sample-to-detector distance, and a spot size of 50 µm × 150 µm. The diffraction images were integrated and processed with GSAS-II. Synchrotron PDF and XRD measurements were measured on selected samples grown on quartz substrates at beamline 11-ID-B at the Advanced Photon Source (APS), Argonne National Laboratory. The data were collected in grazing-incidence geometry with a wavelength of 0.1432 Å. The data were integrated using GSAS-II; PDFs were generated using xPDFsuite with $Q_{max} = 25$ $Å^{-1}$; and PDF fitting was performed in PDFgui[47]. LeBail fits were performed on the XRD data with Topas v.6 in s.g. 225 ($Fm\bar{3}m$). The lattice parameter (a) and sample displacement were refined. Peak shapes were fitted with a Thompson-Cox-Hastings pseudo-Voigt function, with the background fitted to a ten-term polynomial.

Theoretical

The first-principles random structure sampling method entails creating a large number of structures with: (1) random lattice vectors and atomic positions, (2) fixed stoichiometry (for example, $MgMoN_2$) and (3) a fixed number of atoms ($N = 24$). These structures are subsequently relaxed to the closest local minimum on the PES using density functional theory, and then grouped into classes of equivalent structures. The number of structures belonging to each class, or its frequency of occurrence in the structure sampling, is then taken as the size of a corresponding local minimum on the PES and used in the statistical mechanics treatment of the results. An initial pathway for the proposed mechanism for the transformation from RS to RL was computed via atom-to-atom mapping[39]. The PDF $g(r)$ for the theoretical representation of $MgMoN_2$ is directly calculated in real space[48].

The first-principles structure sampling, which is used for structure predictions in this work, proceeds according to the following protocol. In the first step, a large number of structures are generated with random lattice parameters (a,b,c,α,β) using an algorithm that ensures cation–anion coordination[33]. A total of 5,000 structure samples are constructed for $MgMoN_2$, and 2,000 structures for $MgWN_2$ and the other studied nitride materials. In the second step all random structures are relaxed, including the cell parameters and atomic positions, using density functional theory, to the closest local minimum, following the steepest descent algorithms as implemented in VASP computer code[49] within the projector augmented wave formalism using a soft pseudopotential for nitrogen and normal pseudopotentials for all metals. This choice of pseudopotentials balances computational efficiency and structural accuracy. A Monkhorst–Pack k-point grid with the subdivision determined by the VASP $R_k = 20$ parameter and a plane-wave cut-off of 340 eV are used. Automatic k-point grid generation with length parameter $R_k = 20$ enables consistent k-grid density for the random sampling, in which structures are initialized with random lattice vectors. Relaxations are considered converged when the forces on atoms are all below 0.01 eV $Å^{-1}$ and the final pressure is below 3 kbar.

The relaxed structures are grouped into classes having the same underlying (parent) crystal structure. The classification is performed based on (1) the space group assignment of the equivalent structure in which all of the cations (magnesium and molybdenum in the case of $MgMoN_2$) are labelled the same, and (2) the first shell coordination of the atoms. For the samples grouped into classes with the same underlying structure, partition functions and corresponding configurational free energies are then evaluated as a function of temperature using energy per formula unit in the Boltzmann exponents[35]. To analyse the local cation ordering in different predicted disordered RS-$MgMoN_2$ structure variants, each structure was scanned for reproduction of the M–M distances and bond angles in the cation-layered RS motif, followed by visual verification of the specific arrangement of diagonal edge-sharing M-centred octahedra.

To calculate the PDF $g(r)$ in real space[48], for each of the 314 RS-type structures obtained from the random structure sampling, we compute the atom-type-pair-specific PDFs $g_{\alpha}^{S}(r)$, where α and β denote different atom types. The ensemble-averaged $g_{\alpha\beta}(r)$ is then obtained through a sum over each structure S of the ensemble. The total PDF $g(r)$ is then easily obtained as a weighted sum of the partials with the weights coming from an approximation of the X-ray atomic form factors $f_{\alpha}(Q)$. The function mainly used in this work is the reduced PDF $G(r)$ because this can be directly obtained from the Fourier transform of the XRD measurements: $G(r) = 4\pi r n_0(g(r) - 1)$. The partials $G_{\alpha\beta}(r)$ are obtained in a similar way by just replacing $g(r)$ with the appropriate partial $g_{\alpha\beta}(r)$. More details of the PDF calculations are provided in Supplementary Information.

To compute an initial pathway for the proposed mechanism for the transformation from RS to RL, different supercell representations are chosen for the initial and final structures, and combinations of cells with maximum volume overlap are chosen for further analysis[39]. For each choice of cells, atoms are matched between the initial and final cell, solving the assignment problem using the Munkres algorithm. We start by modelling a simple transformation as if all cations have the same chemical identity, and then after the mechanism is found we relabel the atoms based on their correspondence between the two structures. In this way, we find a particular ordering in the RS phase that produces the simplest transformation based on our structure mapping. For the ordered structure, the minimum-energy pathway at 0 K was computed using a solid-state nudged elastic band[50] and was considered

converged when forces between images were reduced to 0.1 eV $Å^{-1}$, and the barriers were estimated using the climbing image method. Evaluation of upper bounds for the barrier for transformation with disorder were performed by performing site swaps between magnesium and molybdenum in $1 \times 1 \times 2$, $1 \times 2 \times 1$ and $2 \times 1 \times 1$ supercells. Energies of images along these pathways are computed without any relaxations, and therefore represent an upper bound of the energy relative to that which would be found using a solid-state nudged elastic band. Under cation-disordered conditions, the rate-determining step is the inversion of the octahedra rather than the shift of the nitrogen atoms, but the barrier associated with this step remains approximately 90 meV per atom or less. When all layers contain 50% molybdenum and 50% magnesium (red line in Supplementary Fig. 7), some of the site swaps associated with this model increase rather than decrease the energy of the RL structure to above its associated RS structure.

Data availability

The data used in the graphs are published in Supplementary Information alongside the paper. Datasets for XRD, AES, PDF and nanocalorimetry figures are also available via figshare at https://doi.org/10.6084/m9.figshare.26344993 (ref. 51). Crystal structure figure files are available via figshare at https://doi.org/10.6084/m9.figshare.26345092 (ref. 52).

References

1. Fleming, G. R. & Ratner, M. A. Grand challenges in basic energy sciences. *Phys. Today* **61**, 28–33 (2008).
2. Kreider, M. E. et al. Nitride or oxynitride? Elucidating the composition–activity relationships in molybdenum nitride electrocatalysts for the oxygen reduction reaction. *Chem. Mater.* **32**, 2946–2960 (2020).
3. Nakamura, Y. et al. Superconducting qubits consisting of epitaxially grown NbN/AlN/NbN Josephson junctions. *Appl. Phys. Lett.* **99**, 212502 (2011).
4. Jiang, K. et al. Mechanical cleavage of non-van der Waals structures towards two-dimensional crystals. *Nat. Synth.* **2**, 58–66 (2022).
5. Zhang, K., Feng, Y., Wang, F., Yang, Z. & Wang, J. Two dimensional hexagonal boron nitride (2D-hBN): synthesis, properties and applications. *J. Mater. Chem. C* **5**, 11992–12022 (2017).
6. Shur, M., Gelmont, B. & Asif Khan, M. Electron mobility in two-dimensional electron gas in AlGaN/GaN heterostructures and in bulk GaN. *J. Electron. Mater.* **25**, 777–785 (1996).
7. Biswas, A., Natu, V. & Puthirath, A. B. Thin-film growth of MAX phases as functional materials. *Oxf. Open Mater. Sci.* **1**, itab020 (2020).
8. Lim, K. R. G. et al. Fundamentals of MXene synthesis. *Nat. Synth.* **1**, 601–614 (2022).
9. Yamane, H. & DiSalvo, F. J. Sodium flux synthesis of nitrides. *Prog. Solid State Chem.* **51**, 27–40 (2018).
10. Niewa, R., Zherebtsov, D. A., Schnelle, W. & Wagner, F. R. Metal–metal bonding in $ScTaN_2$. A new compound in the system ScN–TaN. *Inorg. Chem.* **43**, 6188–6194 (2004).
11. Pilemalm, R., Pourovskii, L., Mosyagin, I., Simak, S. & Eklund, P. Thermodynamic stability, thermoelectric, elastic and electronic structure properties of $ScMN_2$-type (M=V, Nb, Ta) phases studied by ab initio calculations. *Condens. Matter* **4**, 36 (2019).
12. Brokamp, T. & Jacobs, H. Darstellung und Struktur einiger Gemischtvalenter ternärer Tantalnitride mit Lithium und Magnesium. *J. Alloys Compd.* **183**, 325–344 (1992).
13. Verrelli, R. et al. On the study of Ca and Mg deintercalation from ternary tantalum nitrides. *ACS Omega* **4**, 8943–8952 (2019).
14. Gregory, D. H. et al. Layered ternary transition metal nitrides; synthesis, structure and physical properties. *J. Alloys Compd.* **317–318**, 237–244 (2001).
15. Gregory, D. H. Structural families in nitride chemistry. *J. Chem. Soc. Dalton Trans.* **7**, 259–270 (1999).
16. Zakutayev, A., Bauers, S. R. & Lany, S. Experimental synthesis of theoretically predicted multivalent ternary nitride materials. *Chem. Mater.* **34**, 1418–1438 (2022).
17. Greenaway, A. L. et al. Ternary nitride materials: fundamentals and emerging device applications. *Annu. Rev. Mater. Res.* **51**, 591–618 (2021).
18. Bauers, S. R. et al. Ternary nitride semiconductors in the rocksalt crystal structure. *Proc. Natl Acad. Sci. USA* **116**, 14829–14834 (2019).
19. Yang, M. et al. Anion order in perovskite oxynitrides. *Nat. Chem.* **3**, 47–52 (2010).
20. Kageyama, H. et al. Expanding frontiers in materials chemistry and physics with multiple anions. *Nat. Commun.* **9**, 772 (2018).
21. Bem, D. S., Lampe-Önnerud, C. M., Olsen, H. P. & zur Loye, H.-C. Synthesis and structure of two new ternary nitrides: $FeWN_2$ and $MnMoN_2$. *Inorg. Chem.* **35**, 581–585 (1996).
22. Cao, B., Veith, G. M., Neuefeind, J. C., Adzic, R. R. & Khalifah, P. G. Mixed close-packed cobalt molybdenum nitrides as non-noble metal electrocatalysts for the hydrogen evolution reaction. *J. Am. Chem. Soc.* **135**, 19186–19192 (2013).
23. Verrelli, R. et al. On the viability of Mg extraction in $MgMoN_2$: a combined experimental and theoretical approach. *Phys. Chem. Chem. Phys.* **19**, 26435–26441 (2017).
24. Wang, L. et al. Solid state synthesis of a new ternary nitride $MgMoN_2$ nanosheets and micromeshes. *J. Mater. Chem.* **22**, 14559–14564 (2012).
25. Woods-Robinson, R. et al. Role of disorder in the synthesis of metastable zinc zirconium nitrides. *Phys. Rev. Mater.* **6**, 043804 (2022).
26. Arca, E. et al. Redox-mediated stabilization in zinc molybdenum nitrides. *J. Am. Chem. Soc.* **140**, 4293–4301 (2018).
27. Rom, C. L. et al. Bulk and film synthesis pathways to ternary magnesium tungsten nitrides. *J. Mater. Chem. C* **11**, 11451–11459 (2023).
28. Huang, H., Jin, K. H. & Liu, F. Alloy engineering of topological semimetal phase transition in $MgTa_{2-x}Nb_x$. *Phys. Rev. Lett.* **120**, N3 (2018).
29. Wu, Q., Piveteau, C., Song, Z. & Yazyev, O. V. $MgTa_2N_3$: a reference Dirac semimetal. *Phys. Rev. B* **98**, 081115 (2018).
30. Bordeenithikasem, P. et al. Determination of critical cooling rates in metallic glass forming alloy libraries through laser spike annealing. *Sci. Rep.* **7**, 7155 (2017).
31. Tholander, C., Andersson, C. B. A., Armiento, R., Tasnádi, F. & Alling, B. Strong piezoelectric response in stable $TiZnN_2$, $ZrZnN_2$, and $HfZnN_2$ found by ab initio high-throughput approach. *J. Appl. Phys.* **120**, 225102 (2016).
32. Jones, E. B. & Stevanović, V. Polymorphism in elemental silicon: probabilistic interpretation of the realizability of metastable structures. *Phys. Rev. B* **96**, 184101 (2017).
33. Stevanović, V. Sampling polymorphs of ionic solids using random superlattices. *Phys. Rev. Lett.* **116**, 075503 (2016).
34. Jankousky, M., Garrity, E. M. & Stevanović, V. Polymorphism of group-IV carbides: structures, (meta)stability, electronic, and transport properties. *Phys. Rev. Mater.* **7**, 053606 (2023).
35. Jones, E. B. & Stevanović, V. The glassy solid as a statistical ensemble of crystalline microstates. *NPJ Comput. Mater.* **6**, 56 (2020).
36. Ndione, P. F. et al. Control of the electrical properties in spinel oxides by manipulating the cation disorder. *Adv. Funct. Mater.* **24**, 610–618 (2014).
37. Shirzad, K. & Viney, C. A critical review on applications of the Avrami equation beyond materials science. *J. R. Soc. Interface* **20**, 20230242 (2023).

38. Yi, F. & Lavan, D. A. Nanocalorimetry: exploring materials faster and smaller. *Appl. Phys. Rev.* **6**, 031302 (2019).
39. Stevanović, V. et al. Predicting kinetics of polymorphic transformations from structure mapping and coordination analysis. *Phys. Rev. Mater.* **2**, 033802 (2018).
40. Todd, P. K., Fallon, M. J., Neilson, J. R. & Zakutayev, A. Two-step solid-state synthesis of ternary nitride materials. *ACS Mater. Lett.* **3**, 1677–1683 (2021).
41. Kertesz, M. & Hoffmann, R. Octahedral vs. trigonal-prismatic coordination and clustering in transition-metal dichalcogenides. *J. Am. Chem. Soc.* **106**, 3453–3460 (1984).
42. Shang, K. et al. Tolerance factor and phase stability of the $KCoO_2$-type AMN_2 nitrides. *Inorg. Chem.* **63**, 4168–4175 (2024).
43. Shiraishi, A. et al. Design, synthesis, and optoelectronic properties of the high-purity phase in layered $AETMN_2$ (AE=Sr, Ba; TM=Ti, Zr, Hf) semiconductors. *Inorg. Chem.* **61**, 6650–6659 (2022).
44. Talley, K. R. et al. COMBIgor: data-analysis package for combinatorial materials science. *ACS Comb. Sci.* **21**, 537–547 (2019).
45. Zakutayev, A. et al. An open experimental database for exploring inorganic materials. *Sci. Data* **5**, 180053 (2018).
46. Yazawa, K. et al. Anomalously abrupt switching of wurtzite-structured ferroelectrics: simultaneous non-linear nucleation and growth model. *Mater. Horiz.* **10**, 2936–2944 (2023).
47. Farrow, C. L. et al. PDFfit2 and PDFgui: computer programs for studying nanostructure in crystals. *J. Phys. Condens. Matter* **19**, 335219 (2007).
48. Keen, D. A. A comparison of various commonly used correlation functions for describing total scattering. *J. Appl. Crystallogr.* **34**, 172–177 (2001).
49. Kresse, G. & Joubert, D. From ultrasoft pseudopotentials to the projector augmented-wave method. *Phys. Rev. B* **59**, 1758 (1999).
50. Sheppard, D., Xiao, P., Chemelewski, W., Johnson, D. D. & Henkelman, G. A generalized solid-state nudged elastic band method. *J. Chem. Phys.* **136**, 74103 (2012).
51. Zakutayev A. Datasets figures with chemical composition, long-range structure, short-range structure, and structural transformation of layered ternary nitrides. *figshare* https://doi.org/10.6084/m9.figshare.26344993 (2024).
52. Zakutayev A. Crystal structure figures for layered ternary nitrides. *figshare* https://doi.org/10.6084/m9.figshare.26345092 (2024).

Acknowledgements

This work was authored in part at the National Renewable Energy Laboratory (NREL), operated by the Alliance for Sustainable Energy, LLC, for the US Department of Energy (DOE) under contract number DE-AC36-08GO28308. Funding was provided by the Office of Science (SC), Basic Energy Sciences (BES), Materials Chemistry programme, as a part of the Early Career Award 'Kinetic Synthesis of Metastable Nitrides' (experimental results), with contribution from NSF career award number DMR-1945010 (computational results). Nanocalorimeter fabrication was performed in part at the NIST Center for Nanoscale Science & Technology (CNST). Use of the Stanford Synchrotron Radiation Lightsource, SLAC National Accelerator Laboratory is supported by the DOE's SC, BES under contract number DE-AC02-76SF00515. This research used resources of the Advanced Photon Source, a US DOE Office of Science user facility operated for the DOE Office of Science by Argonne National Laboratory under contract number DE-AC02-06CH11357. R.W.S. acknowledges support from the Director's Fellowship within NREL's Laboratory Directed Research and Development programme. We thank C. Perkins for help with AES analysis; N. Strange for assistance with SSRL data collection; U. Ruett and M. Miller for assistance with APS data collection; and B. Julien and K. Yazawa for useful discussions. This work used high-performance computing resources located at NREL and sponsored by the Office of Energy Efficiency and Renewable Energy. Certain commercial equipment, instruments or materials are identified in this document. Such identification does not imply recommendation or endorsement by the National Institute of Standards and Technology (NIST), nor does it imply that the products identified are necessarily the best available for the purpose. The views expressed in the article do not necessarily represent the views of the DOE or the US Government.

Author contributions

A.Z., Y.F., C.L.R., S.R.B., O.B., D.A.L. and R.W.S. conducted experimental measurements. M.J., L.W. and V.S. performed theoretical calculations. A.Z. conceived the study, synthesized the materials, supervised the work and wrote the paper with edits from R.W.S., M.J., L.W., V.S. and all other coauthors.

Competing interests

The authors declare no competing interests.

Additional information

Supplementary information The online version contains supplementary material available at https://doi.org/10.1038/s44160-024-00643-0.

Correspondence and requests for materials should be addressed to Andriy Zakutayev.

Peer review information *Nature Synthesis* thanks Xiaojun Kuang and the other, anonymous, reviewer(s) for their contribution to the peer review of this work. Primary Handling Editor: Alexandra Groves, in collaboration with the *Nature Synthesis* team.